

## Plasma morphology and induced airflow characterization of a DBD actuator with serrated electrode

This article has been downloaded from IOPscience. Please scroll down to see the full text article.

2013 J. Phys. D: Appl. Phys. 46 125204

(<http://iopscience.iop.org/0022-3727/46/12/125204>)

View [the table of contents for this issue](#), or go to the [journal homepage](#) for more

Download details:

IP Address: 194.167.30.129

The article was downloaded on 14/03/2013 at 07:46

Please note that [terms and conditions apply](#).

# Plasma morphology and induced airflow characterization of a DBD actuator with serrated electrode

R Jousot<sup>1,2,3</sup>, A Leroy<sup>1</sup>, R Weber<sup>1</sup>, H Rabat<sup>2</sup>, S Loyer<sup>1</sup> and D Hong<sup>2</sup>

<sup>1</sup> PRISME, UPRES 4229, Université d'Orléans, 8 rue Léonard de Vinci, 45072, Orléans Cedex 2, France

<sup>2</sup> GREMI, UMR 7344, CNRS–Université d'Orléans, 14 rue d'Issoudun, 45067, Orléans Cedex 2, France

E-mail: [annie.leroy@univ-orleans.fr](mailto:annie.leroy@univ-orleans.fr)

Received 22 October 2012, in final form 27 December 2012

Published 25 February 2013

Online at [stacks.iop.org/JPhysD/46/125204](http://stacks.iop.org/JPhysD/46/125204)

## Abstract

Plasma morphology and airflow induced by a dielectric barrier discharge (DBD) actuator, whose exposed electrode geometry is designed with a serrated configuration, are investigated in quiescent air and compared with a DBD actuator consisting of electrodes designed with a standard linear strip configuration. ICCD imaging, electrical measurements and three-component laser Doppler velocimetry were carried out to compare various features of these two actuators. With the serrated configuration, ICCD images of the discharge show that streamers are bent, whereas with the linear configuration they are straight. These curved streamers induce a three-dimensional flow topology, which is confirmed by friction line visualization and velocity measurements. Whereas a two-dimensional wall-jet is induced with the linear configuration, a transverse velocity component is measured with the serrated configuration, implying the creation of spanwise-periodic vorticity. Phase-averaged velocity measurements allow the temporal variation of this transverse velocity to be highlighted. On both sides of a tooth, it has qualitatively the same variation as the longitudinal velocity with respect to the negative or positive half-cycles of the high voltage signal. Moreover, with the same electrical operating parameters, the measured longitudinal velocity was higher, particularly at the tips.

(Some figures may appear in colour only in the online journal)

## 1. Introduction

Plasma actuators can be used to perform active flow control in order to improve the aerodynamic performance of vehicles. Actuators which use a surface dielectric barrier discharge (DBD) are widely studied since they consist of quite simple devices. They are made of a dielectric plate on which metallic electrodes are placed on each side. Supplied by an ac high voltage, a non-thermal plasma is created on the surface of the actuator where charged species drift along the electric field lines and collide with the particles of the surrounding air. As momentum is transferred from the plasma to the air, a flow of a few  $\text{m s}^{-1}$  called ionic wind is induced. Reviews on flow

control by plasma actuators were conducted by Moreau [1], and by Corke *et al* [2] specifically for DBD actuators.

In quiescent air, a typical DBD plasma actuator (i.e. with strip electrodes, called linear design) produces a phase-locked two-dimensional wall-jet with a relatively low velocity. Many studies have therefore been conducted to increase the ionic wind velocity in order to improve the efficiency of plasma actuators when they are used to perform flow control. To achieve this goal, different geometric or electrical parameters can be modified. In the numerous studies available in the literature, the following parameters have been studied: electrode gap [3], length of the grounded electrode [3–6], dielectric thickness [3, 6, 7], dielectric [3, 6–9] and electrode [10] materials, electrode arrangement [11], electrode shape [4, 6, 12–16], and waveform signals [4, 6, 9, 12, 17, 18]. Modification of the shape of the exposed electrode seems to

<sup>3</sup> Present address: PRISME, UPRES 4229, Université d'Orléans, 8 rue Léonard de Vinci, 45072, Orléans Cedex 2, France

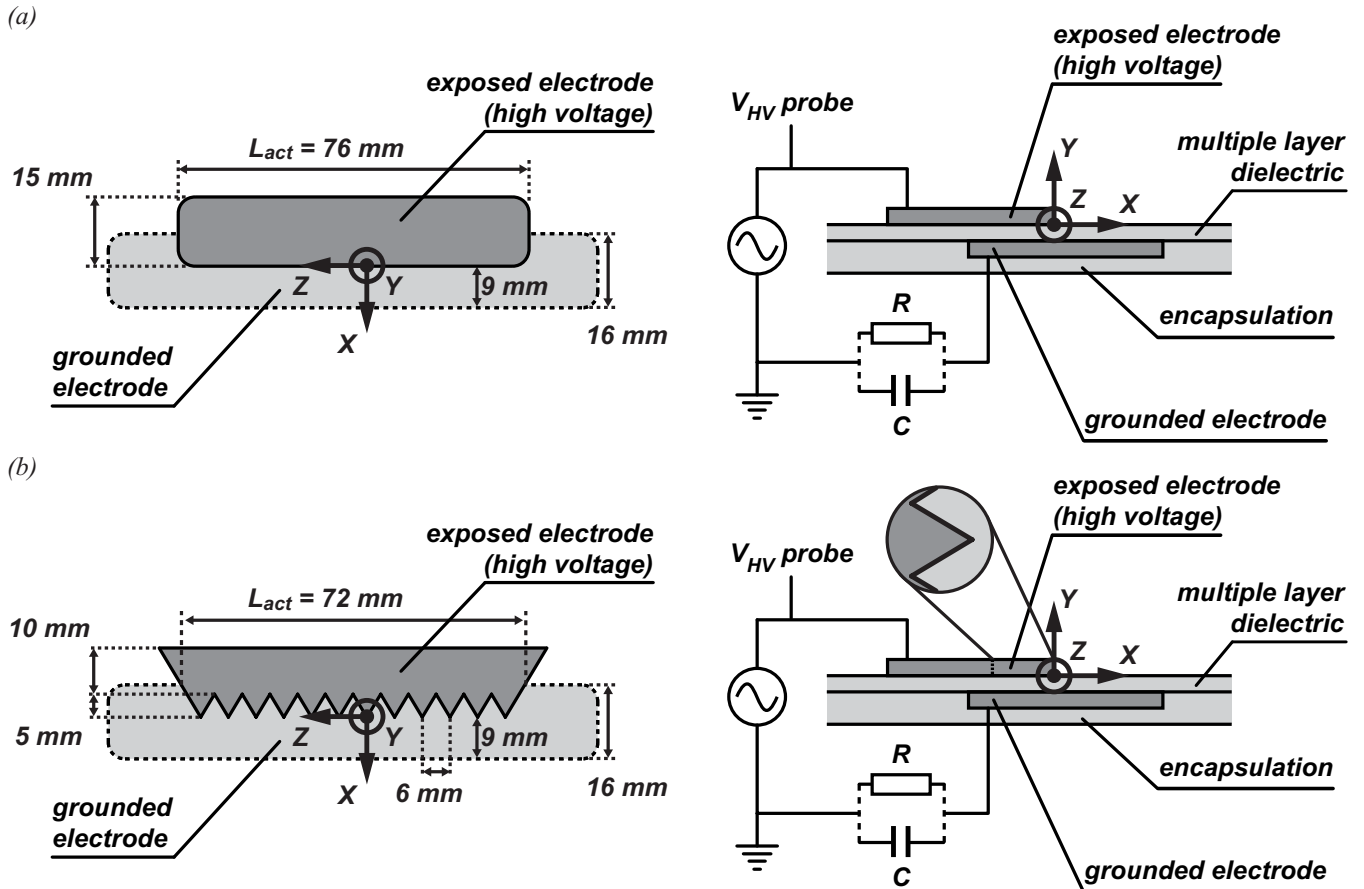


Figure 1. Schematics of (a) the linear and (b) the serrated plasma actuator designs.

be one of the most useful techniques to significantly increase the induced thrust, since an exposed electrode with a sharp edge locally increases the electric field and therefore the ionic wind velocity near the edge. Mesh electrodes with pointed tips [12] or with a serrated edge consisting of triangular patterns in series [6, 16, 19–22] can be used. These serrated designs lead to an increase in the mean thrust up to 50% higher than for a strip electrode [6, 12]. Moreover, this type of electrode design can produce a three-dimensional flow topology [14, 20], which can be interesting for aerodynamic control applications. Different geometric shapes of electrodes have therefore been studied such as serpentine, triangular or square [20, 21] in order to promote a three-dimensional ionic wind. These electrode designs have a pattern forming an alternation of tips and roots. In each case, a three-dimensional flow field is induced in quiescent air, characterized by a ‘pinching’ of the flow at the root and a ‘spreading’ at the tip [14]. These configurations of plasma actuators can generate spanwise-periodic streamwise vortex structures [16, 21].

In this study, a plasma actuator with a sawtooth edge exposed electrode is considered. The serrated design was used rather than a serpentine or a square one in order to induce a three-dimensional ionic wind (due to the periodicity of roots and tips) with an increase in the longitudinal velocity (due to the serration). To combine these flow characteristics, the tooth size was chosen appropriately with a spanwise length/height ratio of  $r = 1.2$ . Previous studies have shown

that a small ratio is beneficial to induce thrust ( $r = 0.25$  in [6] and  $r = 0.5$  in [19]) whereas a large ratio allows the actuator to create vorticity ( $r = 2$  in [16, 21]). The serrated configuration is compared with the plasma actuator with strip electrodes. The plasma morphology of the two designs and the electrical characteristics are studied. Friction line visualizations are presented and introduce, in qualitative terms, the three-dimensional flow topology induced by the serrated design. In order to study the ionic wind quantitatively, a three-component laser Doppler velocimetry (3C-LDV) device is used to map the flow fields induced by serrated and linear designs, in quiescent air. Time-averaged and phase-locked measurements are carried out to characterize the ionic wind both spatially and temporally.

## 2. Experimental setup

### 2.1. Actuator designs

Two actuator configurations are considered herein. The linear design had strip electrodes (figure 1(a)) and is called the standard configuration in this study. The second design had an exposed electrode with a sawtooth edge (figure 1(b)), called the serrated configuration. The grounded electrode was not modified. In both cases, the actuator was composed of two metallic electrodes separated by a dielectric panel, which consisted of three layers of two dielectric materials: a  $500 \mu\text{m}$

thick Mylar sheet was placed between two Kapton sheets (55  $\mu\text{m}$  thick), giving an overall thickness of about 610  $\mu\text{m}$ . The electrodes were made of adhesive copper foil tape. The upper exposed electrode was connected to an ac power supply; the lower one was grounded directly or via a measurement component. Kapton was used to encapsulate the grounded electrode in order to inhibit plasma formation on this side. The encapsulation did not affect the ionic wind generation on the upper side [23].

The linear actuator had a rectangular exposed electrode 76 mm in spanwise length ( $Z$ -axis) and 15 mm in width ( $X$ -axis), overlapping the grounded electrode on 5 mm. The serrated actuator had an exposed electrode with a sawtooth edge. It was composed of 12 single triangular patterns, forming an alternation of tips and roots. Each triangle pattern formed a ‘tooth’ 5 mm in height and 6 mm in spanwise length. For both cases, the insulated electrode was 120 mm in length and 16 mm in width.

### 2.2. Electrical and optical diagnostics

In the present experimental setup, the actuator operated in a continuous actuation mode at a frequency ( $f_{HV}$ ) of 1 kHz. The driving voltage amplitude ( $V_{HV}$ ) was set to 10 kV, except for the measurement of the active power achieved as a function of the high voltage amplitude. A high voltage probe (Tektronix Series P6015A, 75 MHz, 3.0 pF) was used to measure the voltage applied to the actuator. A carbon-film resistor ( $R = 47 \Omega$ , 5%, 1 W) was set up to measure the discharge current through the actuator, and a silvered-mica capacitor ( $C = 47 \text{ nF}$ , 1%, 500 V) measuring the charges crossing the actuator was used to determine the power consumption of the running actuator. The resistor and the capacitor were not wired simultaneously. The probe capacitance was three orders higher than the actuator capacitance in order to optimize the measurement of charges crossing the actuator [7, 24]. The active power was assessed over 6000 discharge cycles by the Lissajous method with 502 data points recorded (at 500 kHz) per discharge cycle. The electrical signals were monitored on a digital oscilloscope (LeCroy WaveSurfer Series, 64 Xs-A, 600 MHz, 2.5 Gs  $\text{s}^{-1}$ , 8 bits).

Images of the discharge were recorded by an intensified CCD camera (Andor iStar DH734) equipped with a lens 60 mm in focal length ( $f/2.8$ ). The camera was triggered using a pulse synchronized with the high voltage. The discharge was imaged during both positive and negative half-cycles.

### 2.3. Three-component laser Doppler velocimetry

The velocity measurements were carried out using a 3C-LDV TSI system. A 15 W ionized Ar laser (Spectra Physics, Series 2000) provided beams to two probes of 363 mm in focal length (probes A and B in figure 2), operating in back-scatter mode. The first probe provided the 532 nm and the 488 nm wavelength beams, the second one the 476.5 nm wavelength beams.

The probes were rigidly and horizontally mounted on a support. To ensure only one velocity measurement location, the alignment of the three LDV volumes was checked with a pinhole. The actuator was placed on a moving support

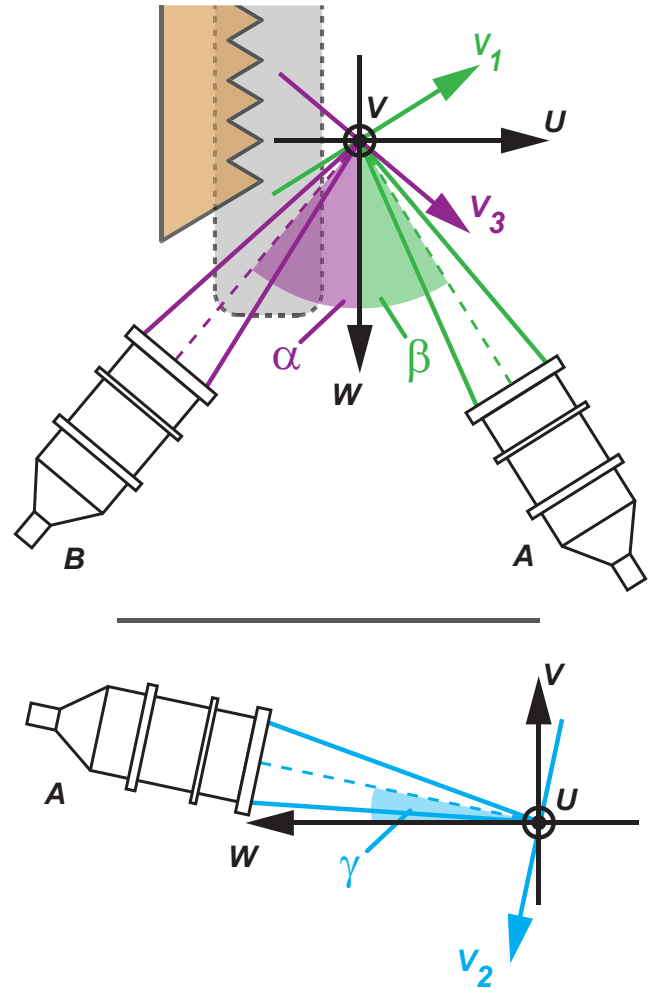


**Figure 2.** Schematic of the probes arrangement (A and B) of the 3C-LDV system.

inside a closed box measuring  $0.5 \times 0.5 \times 1 \text{ m}^3$  (see [25] for further details). A 3-axis traversing system ensured the displacement of the actuator with a resolution step on each axis of 0.1 mm and a precision of  $\pm 0.02 \text{ mm}$  on each position. The position of the LDV measurement volumes crossing the dielectric surface was checked in order to determine the height of the first measurement point. A 10 s pause was added after each displacement of the actuator in order to avoid any vibrations during measurement. The closed box was seeded with olive oil droplets produced by an aerosol generator.

The mean droplet diameter was around  $1 \mu\text{m}$  according to the manufacturing data, ensuring a characteristic response time of the droplets of about  $2.8 \mu\text{s}$  [26]. This relaxation time ensured that droplets were able to follow the flow fluctuations up to 8 kHz with a precision of at least 1%. Once the seeding of the box had been achieved, a time delay was observed to obtain quiescent air. Accuracy of the LDV measurements of the mean velocity components ( $U$ ,  $V$  and  $W$ ) was estimated by

$$\varepsilon_x = \frac{t_{N_i-1, 95\%} I_x}{\sqrt{N_i}}, \quad (1)$$

where  $\varepsilon_x$  was the root-mean-square error of a time-averaged velocity component  $x$ ,  $N_i$  was the number of independent

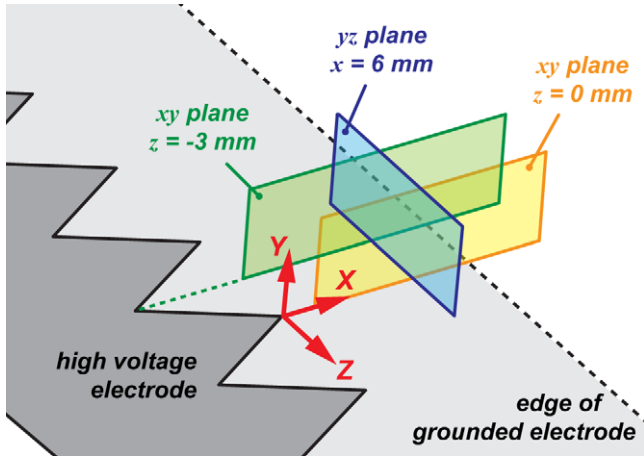


**Figure 3.** Schematic of the three planes considered for the time-averaged velocity measurements.

samples (estimated with  $N_i = 0.5 \times T_{acq} \times f_{forcing}$  [27]),  $t_{N_i-1, 95\%}$  was the quantile of Student's  $t$ -distribution with  $N_i-1$  degrees of freedom and a confidence interval of 95%, and  $I_x$  (relative to the  $x$  component) was the ratio between the standard deviation of the mean velocity and the mean velocity. The median values of  $\varepsilon_U$ ,  $\varepsilon_V$  and  $\varepsilon_W$ , estimated with all the measurement points, were assessed to 0.44%, 2.22% and 3.85%, respectively. For the time-averaged measurements, the mean data rate of the LDV system was assessed at about 8 kHz for the three velocity components.

An interaction between the seeding particles and the plasma could be expected. Indeed, the particles may be charged and accelerated by stronger Coulombian forces near the dielectric surface. In regards to previous studies [25, 28], it was assumed that the seeding particles were weakly influenced by the electric field inherent to the plasma discharge, since particle-based technique such as LDV is able to capture with good agreement both shape and magnitude of the velocity profiles.

The two LDV probes were placed according to the arrangement shown in figure 2:  $V_1$ ,  $V_2$  and  $V_3$  were the velocity components measured by the probes;  $U$ ,  $V$  and  $W$  were the components in the Cartesian coordinate system  $\{X; Y; Z\}$  defined by the actuator (figure 1). The angles between the two coordinate systems ( $\{V_1; V_2; V_3\}$  and  $\{U; V; W\}$ ) were set at  $\alpha = 19^\circ$ ,  $\beta = 17^\circ$  and  $\gamma = 6^\circ$ . The two probes were angled downwards by angle  $\gamma$  in order to approach measurement volumes that were the closest to the dielectric surface. The velocity components measured by the LDV system were a combination of the Cartesian components and the transformation matrix (2):

$$\begin{bmatrix} V_1 \\ V_2 \\ V_3 \end{bmatrix} = \begin{bmatrix} \cos \beta & 0 & -\sin \beta \\ \sin \gamma \sin \beta & -\cos \gamma & \sin \gamma \cos \beta \\ \cos \alpha & 0 & \sin \alpha \end{bmatrix} \cdot \begin{bmatrix} U \\ V \\ W \end{bmatrix}. \quad (2)$$

In order to describe the flow topology induced by the different plasma actuator designs, velocity profiles were performed within three measurement planes (figure 3): two longitudinal  $xy$ -planes, and a transverse  $yz$ -plane. Origin of

the Cartesian coordinate system was located at the tip of a tooth. The first  $xy$ -plane was aligned on a tip (plane origin at  $O(1.5, 0.2, 0)$  and dimensions of  $dx \times dy = 10.5 \times 2.8 \text{ mm}^2$ ) and the second one on a root ( $O(1.5, 0.2, -3)$  and  $dx \times dy = 10.5 \times 2.8 \text{ mm}^2$ ). The  $yz$ -plane was set at the longitudinal position of  $x = 6 \text{ mm}$  ( $O(6, 0.2, -6)$  and  $dy \times dz = 3.8 \times 9 \text{ mm}^2$ ), and was chosen to highlight the three-dimensional behaviour of the ionic wind induced with the serrated design. With the discrete measurement points, a 2D interpolation was performed in order to obtain the flow fields. The displacement steps varied according to  $\delta x = 1.5\text{--}3 \text{ mm}$ ,  $\delta y = 0.1\text{--}0.5 \text{ mm}$  and  $\delta z = 1$  to  $1.1 \text{ mm}$  within the measurement planes.

#### 2.4. Friction line visualizations

Friction line visualizations on the actuator surface were performed using a viscous coating made of oleic acid, dodecane, silicon oil and titanium dioxide according to [29]. This technique allows the three-dimensional flow topology to be described from specific coating patterns at the body surfaces [30, 31]. The wall was coated with the mixture using a brush. The plasma actuator was then ignited with fixed electrical parameters until the friction lines became visible. Shaped lines created by the coating displacement were representative of wall streamlines. During electrical discharges streamers occurred close to the surface and could influence friction line patterns. Consequently, great care was preliminarily taken to check that the coating did not disturb the electrical discharge in terms of electrical characteristics. Focusing on demonstrating the three-dimensional flow topology generated using the serrated design, this technique here provided the possibility to qualitatively compare the flow topology generated using the linear or the serrated designs.

### 3. Discharge characterization

#### 3.1. Plasma morphology

The characteristic structure of the micro-discharges was observed during each active part (i.e. with the plasma present on the dielectric surface) of the two half-cycles (figure 4). For the linear design, the discharge was composed of long, thin and discrete filaments during the positive half-period: the streamers propagated from specific locations on the exposed electrode [32] and were highly filamentary [33]. During the negative half-period, the discharge had a diffuse nature and appeared as corona-type plasma [34], emanating from discrete locations. For the serrated design, the discharge exhibited similar characteristics. Furthermore, the streamers generated with the serrated design were longer than those created with the linear design for the same applied high voltage. This was due to the local increase in the electric field at each tip. The shape of the discharge filaments was also modified: streamers were bent with the serrated design whereas they were straight with the linear one.

The curved shape of streamers came from the geometric repetition of the triangular pattern. For a given tooth, the streamers were ignited at both its edges and they then spread over the surface in a straight and edge-perpendicular direction,

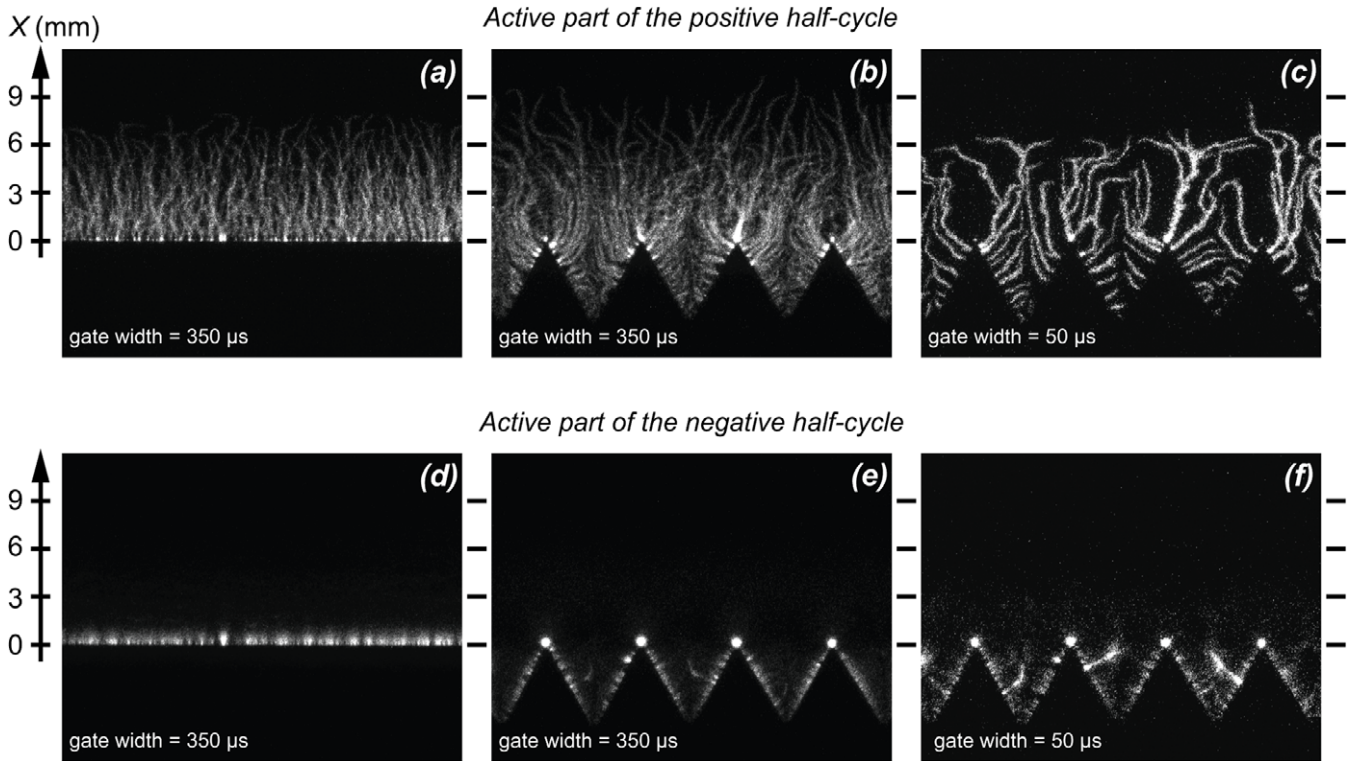


**Figure 4.** Plasma imaging during the active part of: the positive half-cycle for (a) linear and (b), (c) serrated designs, the negative half-cycle for (d) linear and (e), (f) serrated designs ( $V_{HV} = 10\text{ kV}$  and  $f_{HV} = 1\text{ kHz}$ ).

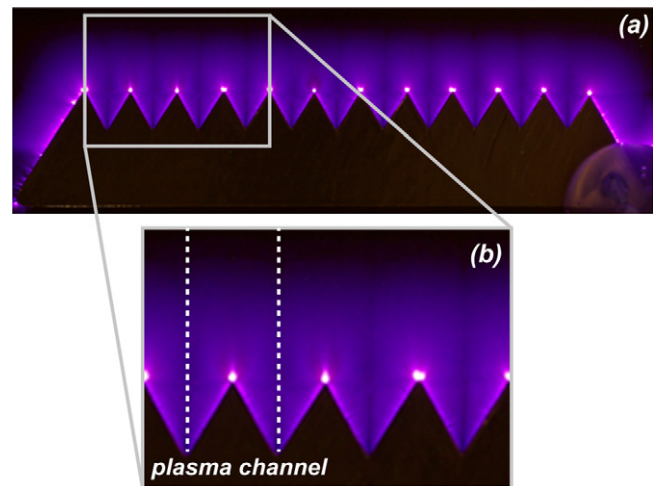
towards the neighbouring teeth. In the vicinity of a root, the streamers ignited from the edge of a given tooth approached those coming from the neighbouring tooth. The streamers pushed each other since their head had the same polarity, and they deviated, giving the plasma filaments a curved shape. If there were enough surface charges on the dielectric, the filaments propagated along the longitudinal direction (i.e. along the  $X$ -axis), otherwise they vanished. Figures 4(c) and (f) show more clearly the deviation of the filaments (images taken  $100\ \mu\text{s}$  after the beginning of the active part).

During the negative half-cycle, the micro-discharges took on the appearance of diffuse corona spots propagating with a plume shape whatever the design considered. The increase in the electric field due to serration was observed since bright spots were located at the tip of each tooth. This could lead to a more effective negative charge deposition that induced the development of longer streamers during the following half-cycle. The corona spots could take on a curved shape like the positive filaments and for the same reasons.

For the serrated design, the plasma was non-uniform along the spanwise direction (figure 5(a)). For each tooth, the discharge was self-limited into a zone delimited by the two longitudinal axes (along the  $X$  direction) aligned on each root (figure 5(b)). These axes were the two boundaries outlining the plasma channel, which was self-limited in the transverse direction ( $Z$ -axis). The photo was taken with a digital camera.

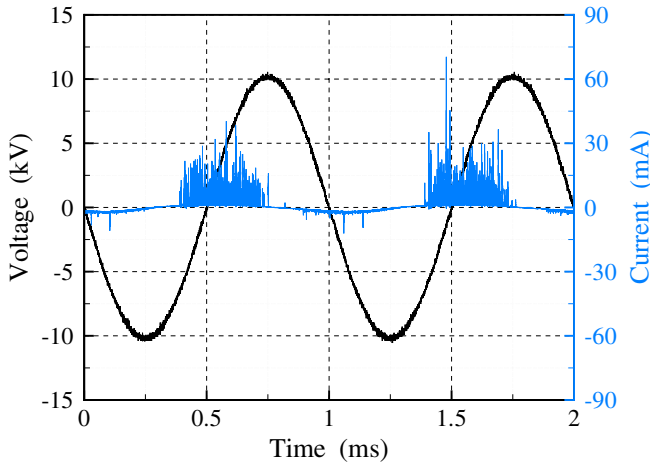
### 3.2. Electrical measurements

Figure 6 shows the instantaneous discharge current for the serrated design. Overall, the current curves exhibited similar



**Figure 5.** Image of the plasma for the serrated design (a) and schematic of a plasma channel (b) (exposure time of 20 s,  $V_{HV} = 10\text{ kV}$ ,  $f_{HV} = 1\text{ kHz}$ ).

patterns for both designs, suggesting that the shape of the exposed electrode had a weak influence on the discharge current features. The discharge current had a near-sinusoidal pattern superimposed with two groups of random peaks for each period. The characteristic structure of the micro-discharges was observed. During the positive half-cycle, streamers were present on the dielectric surface. This is depicted on the current curve by a rapid sequence of numerous peaks. During the negative half-cycle, the number of visible peaks was significantly reduced since instead of streamers, corona spots were observed on the dielectric surface.



**Figure 6.** Instantaneous discharge current and high voltage signals for the serrated design of plasma actuator ( $V_{HV} = 10\text{ kV}$ ,  $f_{HV} = 1\text{ kHz}$ ).

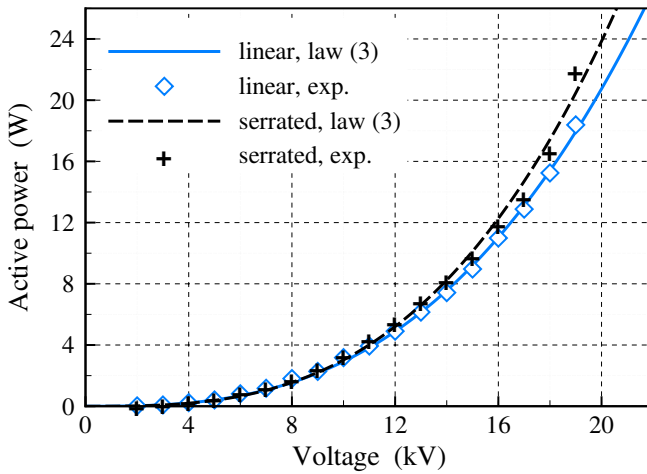


**Figure 7.** Active power versus high voltage amplitude for the linear ( $\diamond$ ) and the serrated ( $+$ ) designs of plasma actuator ( $f_{HV} = 1\text{ kHz}$ ). The symbols are related to the experimental data sets; the lines stand for the power consumption obtained with (3).

Figure 7 shows the power consumption as a function of the high voltage amplitude. For both configurations, the active power evolved as  $P_{el} \propto (V_{HV})^n$ , which was similar to the laws found in previous studies [4, 35]. The active power  $P_{el}$  (W) could be estimated by the empirical law

$$P_{el} = C_{act} f_{HV} L_{act} (V_{HV})^n, \quad (3)$$

where  $C_{act}$  ( $\text{W m}^{-1} \text{Hz}^{-1} \text{V}^{-n}$ ) is a coefficient depending on the geometric arrangement of the actuator,  $f_{HV}$  (Hz) is the actuator frequency,  $L_{act}$  (m) is a characteristic spanwise length of the exposed electrode, and  $V_{HV}$  (V) is the high voltage amplitude. The coefficient  $C_{act}$  and the exponent  $n$  were obtained by fitting (least-squares method) the experimental data. The values of  $L_{act}$ ,  $C_{act}$  and  $n$  used to estimate the active power are summarized in table 1.

For the same applied voltage, the power per unit actuator length ( $P_{el}/L_{act}$ ) of the serrated design was about 16% higher than with the linear one. The increase in the power consumption could be induced by the greater effective length

**Table 1.** Parameters of the empirical power law (3).

Design	$L_{act}$ (m)	$C_{act}$ ( $\text{W m}^{-1} \text{Hz}^{-1} \text{V}^{-n}$ )	$n$	$R^2$
Linear	0.076	$2.25 \times 10^{-13}$	2.81	0.99
Serrated	0.072	$3.84 \times 10^{-14}$	3.01	0.99

of the exposed electrode edge due to its sawtooth-like shape, and by the greater plasma length due to the serration. In addition these greater lengths induced an increased surface of plasma (assessed with ICCD images [36]). Whereas the ratio of  $P_{el}/L_{act}$  between the two designs was constant within the range of voltage amplitude in this study case, the ratio (between the two actuator configurations) of power density per covered area suggested by Kriegseis *et al* [36] was not constant to qualify the increase in the power consumption. Further experiments have to be performed to establish which parameter is the most relevant to explain this power increase.

## 4. Characterization of the induced flow

### 4.1. Qualitative investigation of the ionic wind topology

Friction line visualizations were performed at the surface of the plasma actuator to investigate the main differences in the flow topology generated using the linear or the serrated designs. In order to check that the coating did not disturb the electrical discharge in terms of electrical characteristics, the current was monitored with an oscilloscope. The results showed that the features of the discharge current remained the same as those obtained with an uncoated dielectric surface, suggesting that the discharge was not disrupted by the mixture. In addition, images of the discharge (figures 8(a) and (b)) performed with an ICCD camera revealed that the streamers (and the corona spots) developed in the same manner whatever the surface (coated or uncoated). By comparing the length of the streamers to the signature of the main shaped friction lines (figure 8(c)), one can note that the friction line signatures are still visible downstream the grounded electrode. It can be noted that this visualization technique shows how the flow topology is related to the plasma morphology since both plasma filaments discussed in the last section and friction lines show similar shapes. However, the use of this technique in this experimental study gave a mean to investigate differences in the flow topology generated using the linear or the serrated designs in the region of interest shown in figure 4, downstream the tooth tips, where velocity measurements were carried out.

Whereas no noticeable shapes were observed for the linear design (figure 9(a)) since the induced jet-like flow was fully two-dimensional, for the serrated design, main lines named ‘separatrices’ divided the flow into distinct regions (figures 9(b) and (c)). They appeared aligned on the roots, and extended downstream the grounded electrode. The separatrices were located between plasma ‘channels’ observed on the discharge images. Downstream the teeth, the skin friction lines converged when approaching these separatrices, suggesting that the flow sprang up from the wall [31]. Thus each separatrix, being paired with an ejection of flow, is a

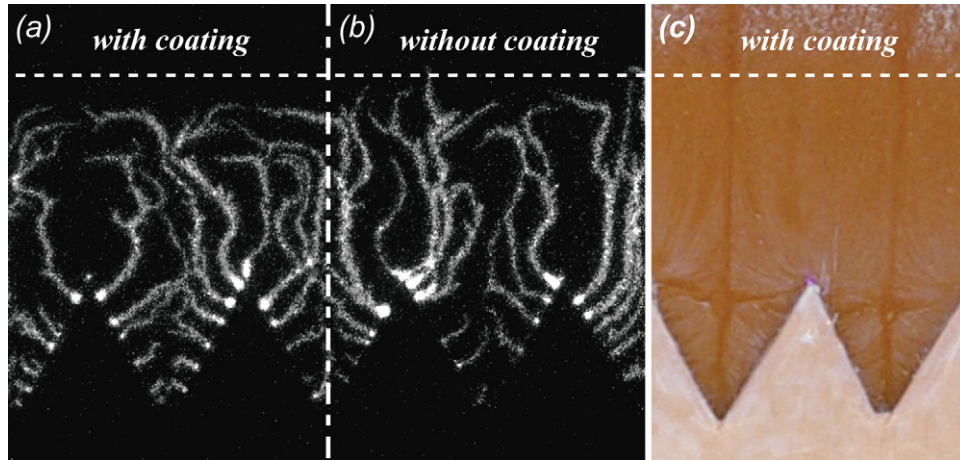


**Figure 8.** Streamer appearance for the serrated design (a) with viscous coating applied on the dielectric surface and (b) without coating. The image ( $600 \mu\text{s}$  gate delay,  $50 \mu\text{s}$  gate width) was recorded 10 s after the actuator was switched on ( $V_{\text{HV}} = 10 \text{ kV}$ ,  $f_{\text{HV}} = 1 \text{ kHz}$ ). (c) The corresponding friction line visualization.

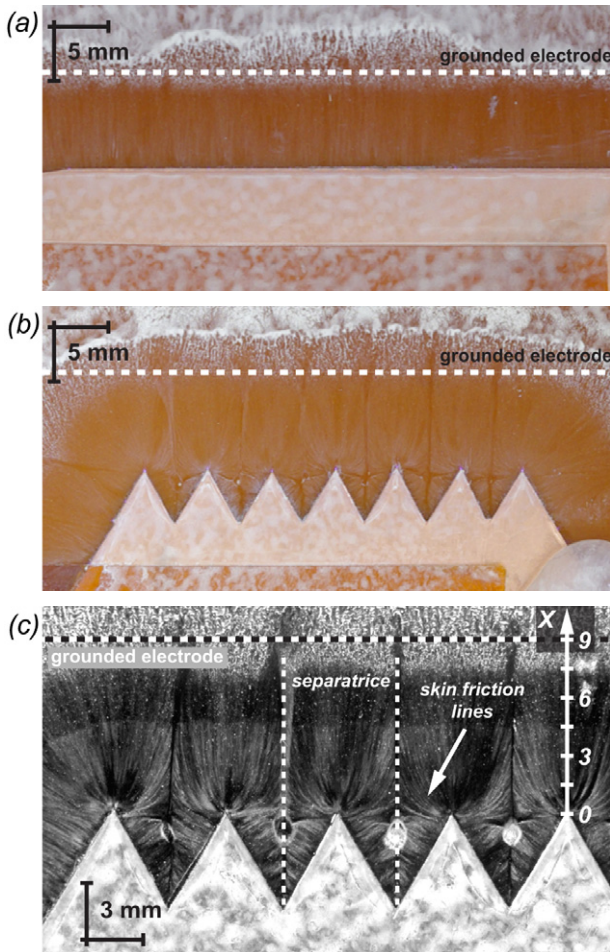


**Figure 9.** Friction line visualizations for (a) linear and (b) serrated designs at  $V_{\text{HV}} = 10 \text{ kV}$  and  $f_{\text{HV}} = 1 \text{ kHz}$ ; (c) close-up of the separatrix for the serrated design (this image was numerically processed to highlight the friction lines).

separation line. The presence of these lines can be due to the convergence of both induced flows emerging from the adjoining edges of two consecutive teeth. This visualization reveals that the flow induced by the serrated design has a

three-dimensional topology downstream the teeth, and more specifically, that the signature of the main expected separation lines is due to counter-rotating vorticity in the flow as shown by analysing flow velocities in the following section.

#### 4.2. Time-averaged flow topology

The time-averaged flow topologies were mapped using 3C-LDV within the three planes introduced previously. As expected, the linear design induced a two-dimensional flow topology (not shown here). Figure 10 shows, for the serrated design, a spanwise variation of the velocity contours in the transverse  $yz$ -plane: similar velocity levels at the tip ( $z = 0 \text{ mm}$ ,  $z = -6 \text{ mm}$ ), and at the root ( $z = 3 \text{ mm}$ ,  $z = -3 \text{ mm}$ ) were noticed. The maximal values of the longitudinal velocity ( $U$ ) were measured at the tip and close to the dielectric surface. This is due to the serration which locally increased the electric field. The transverse velocity ( $W$ ) contours showed that the flow created by the serrated design was three dimensional. The maximal values of the  $W$ -velocity were measured between a tip and a root, as mentioned in a previous study [21]. This is due to the fact that the ionic wind was blown perpendicularly to the tooth edge. Since this velocity component changed signs alternately, with reversals at each tip and root, vorticity ( $\omega_x$ ) was induced (figure 11). The vorticity reversed at the root ( $z = -3 \text{ mm}$ ) and reached its maximum value between the tip and the root where the  $W$ -velocity gradient was the highest. Due to a geometrical effect (hand-cut electrodes), the transverse velocity, and thus the vorticity, could reverse in the vicinity of the root and not exactly at the root. The maxima of  $\omega_x$  ( $\approx \pm 1000 \text{ s}^{-1}$ ) measured in this study were close to those reported by Durscher and Roy [21] for a comparable normalized power ( $P_{\text{el}}/L_{\text{act}} \approx 40 \text{ W m}^{-1}$ ). Near the tip, the vorticity was negligible since the induced flow there was mainly two dimensional.

One can observe that within the plane aligned on a tip ( $z = 0 \text{ mm}$ ), the longitudinal acceleration (along the  $X$ -axis) increased both in strength and length (figures 12(a) and (c)). This can be attributed to serration which led to longer streamers

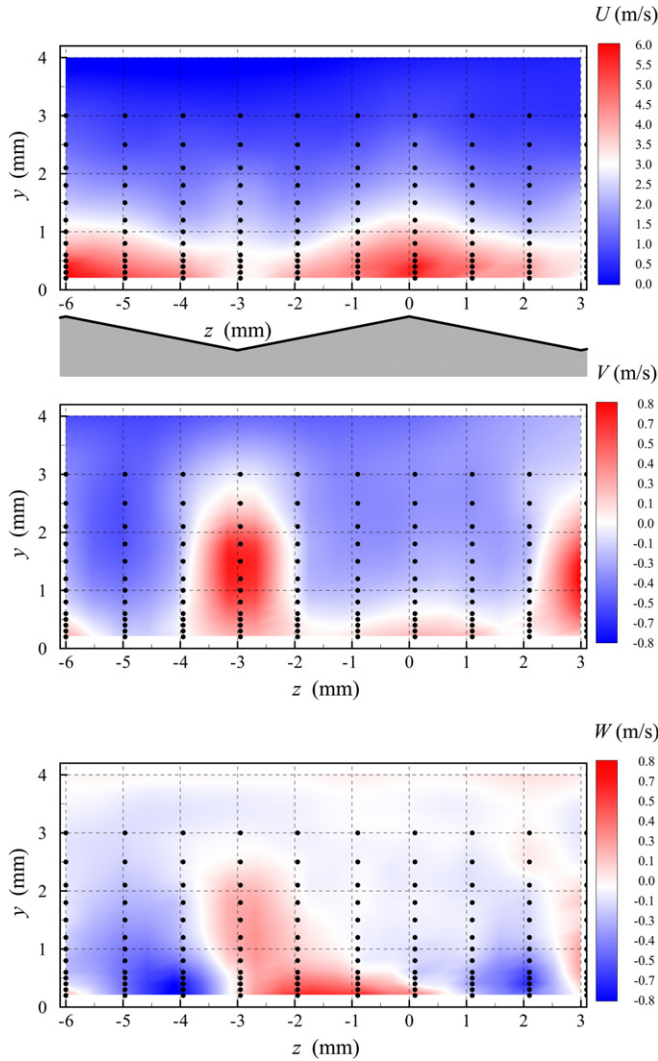


**Figure 10.** Interpolated velocity flow fields in the  $yz$ -plane at  $x = 6$  mm for the serrated design ( $V_{HV} = 10$  kV,  $f_{HV} = 1$  kHz). The black dots stand for the measurement positions.

and corona spots than for the linear design. The  $U$ -velocity was maximal above the plasma region ( $x < 9$  mm) and close to the surface. This longer acceleration was paired with a lower vertical  $V$ -velocity (figures 13(a) and (c)). Thus, the diffusion of the ionic wind for the serrated design was initiated further than the linear one. For a height greater than 1 mm, the  $V$ -velocity was negative. The ambient air was deflected towards the plasma region due to the acceleration of the flow at the dielectric surface, which induced air suction above the discharge.

Within the  $xy$ -plane aligned on a root, the pinching effect [21] induced the highest, and positive, values of the  $V$ -velocity (figure 13(b)). Indeed, this effect was responsible for a lift-up motion: the flow streams induced by two successive teeth collided and were propelled in normal-to-surface ( $y > 0$ ) and in-plane ( $x > 0$ ) direction. This pinching was paired with a decrease in the  $U$ -velocity (figure 12(b)). The low acceleration of the flow was due to the fact that there was no plasma at this particular position. The airflow motion was not induced by a plasma body force but by the merging of flows coming from

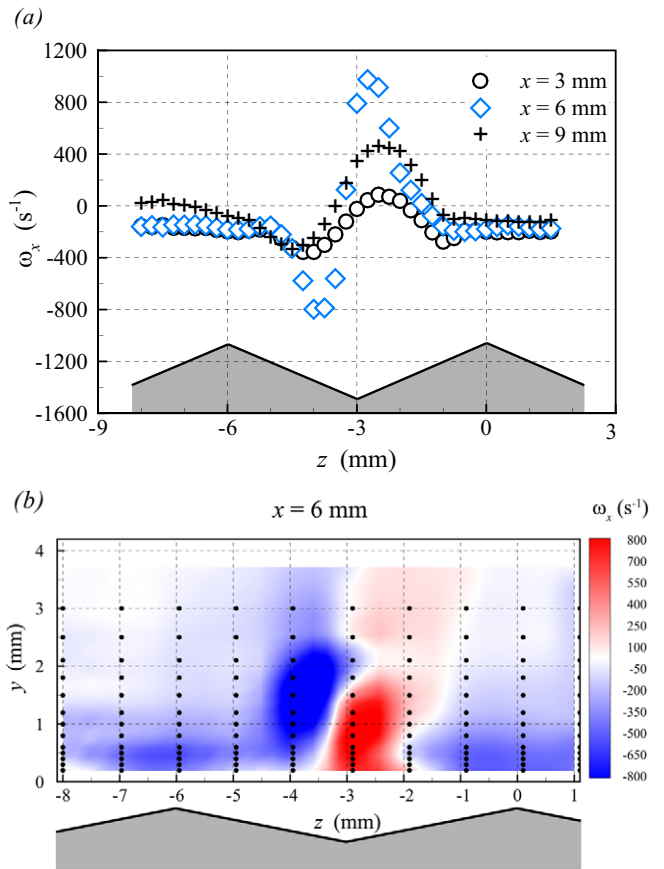


**Figure 11.** Vorticity (a) profile according to the spanwise direction for three longitudinal positions (surface-normal position of  $y = 1$  mm) and (b) interpolated flow field in the  $yz$ -plane at  $x = 6$  mm for the serrated design ( $V_{HV} = 10$  kV,  $f_{HV} = 1$  kHz). The black dots stand for the measurement positions.

adjoining teeth. This flow topology corroborated the presence of separatrices on the friction line visualization.

#### 4.3. Phase-averaged velocity

In this section, the velocity measurements synchronized with the high voltage are discussed. As the mean data rate of the LDV system was around 8 kHz, it was not possible to study the influence of the positive and negative half-cycles of the ac voltage ( $f_{HV} = 1$  kHz) with correct sampling. In order to get round this low data rate, the velocity measurements were phase-locked to the actuator frequency. For each velocity component, at least 90 000 validated counts were recorded, enabling the velocity to be calculated with 500 seeding particles per  $2^\circ$ -phase angle of the sine voltage.

The measurements were made above the discharge ( $x = 3$  and 6 mm) and close to the surface ( $y = 0.5$  mm). The velocity variations during a single cycle were reported in polar coordinates where the radius stands for the velocity magnitude (figure 14). The active part of the negative half-cycle lasted from  $0^\circ$  to  $90^\circ$ , and the positive one from  $180^\circ$  to  $270^\circ$ . Figure 14(a) shows the three velocity components for the serrated (measurement position aligned on a tip) and the linear designs, at  $x = 6$  mm. Figure 14(b) is relative to the serrated

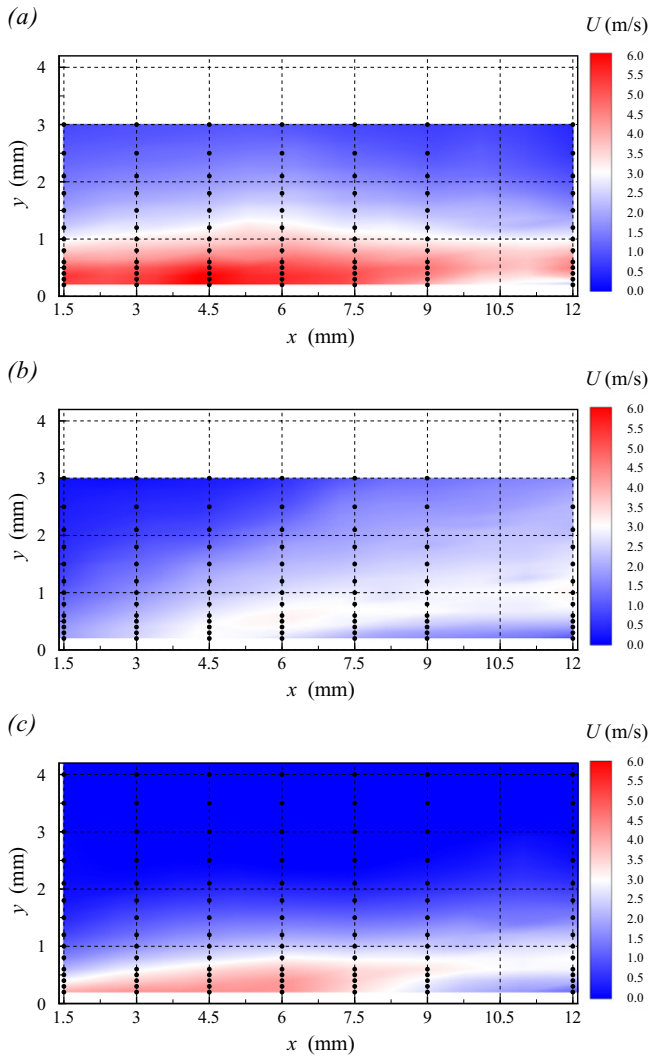


**Figure 12.** Interpolated  $U$ -velocity flow field in  $xy$ -planes: (a) at a tip ( $z = 0$  mm), and (b) at a root ( $z = -3$  mm) for the serrated design and (c) for the linear design ( $V_{HV} = 10$  kV,  $f_{HV} = 1$  kHz). The black dots stand for the measurement positions.

design with measurement points located on either side of a tooth, at  $x = 3$  mm.

The  $U$  and  $V$  components of the ionic wind velocity followed the temporal scenario described in previous studies [3, 18, 25, 37]. During the negative half-cycle ( $0^\circ$ – $180^\circ$ ), the  $U$ -velocity of the ionic wind was higher than during the positive half-cycle ( $180^\circ$ – $360^\circ$ ). For the active part of the negative half-period the flow was accelerated ( $30^\circ$ – $90^\circ$ ), and air suction in the vicinity of the discharge was induced ( $V < 0$ ). For the serrated design, the ionic wind velocity was greater than with the linear design, and the suction duration was slightly increased. In addition, this phase lasted longer for the positions on either side of the tooth (figure 14(b)). For the remainder of the negative half-period, the flow decelerated slightly because of hydrodynamic effects and pressure [18] since the plasma was extinguished on the dielectric surface. At the beginning of the positive half-period, the plasma was reignited, inducing a deceleration of the  $U$ -velocity ( $180^\circ$ – $210^\circ$ ). This deceleration was paired with a significant increase in the  $V$ -velocity, probably induced by the reversal motion of the

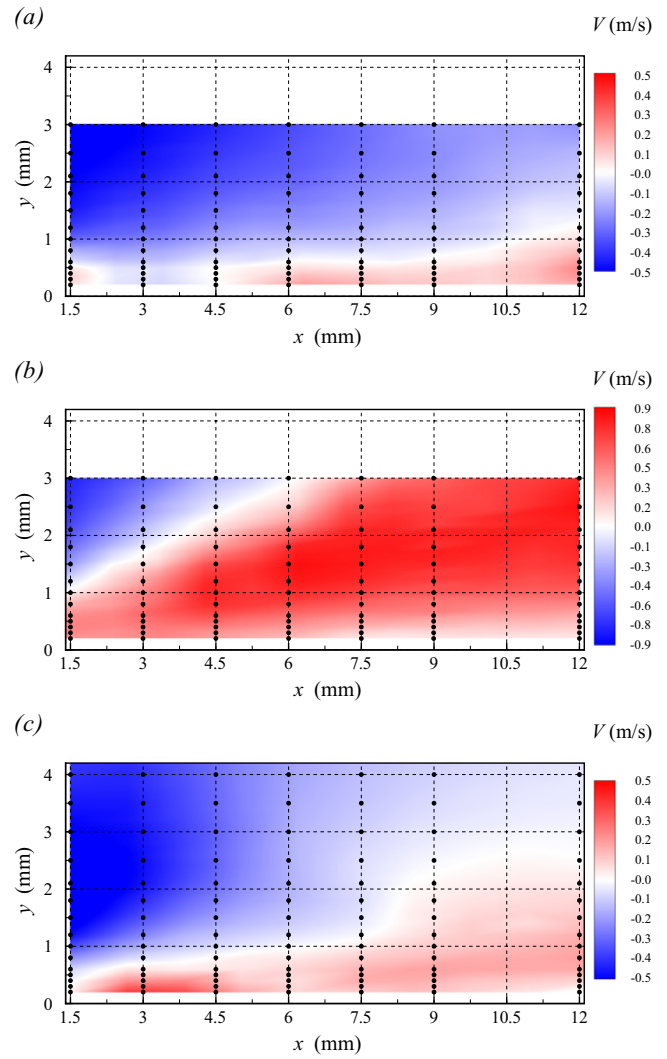


**Figure 13.** Interpolated  $V$ -velocity flow field in the  $xy$ -planes: (a) at a tip ( $z = 0$  mm) and (b) at a root ( $z = -3$  mm) for the serrated design and (c) for the linear design ( $V_{HV} = 10$  kV,  $f_{HV} = 1$  kHz). The black dots stand for the measurement positions.

electrical charges accumulated on the dielectric surface during the previous half-period [4, 38]. Then, the positive ions drifted downstream and dominated the momentum transfer to the air until the active part of the positive half-cycle ended. An acceleration of the  $U$ -velocity was measured ( $210^\circ$ – $270^\circ$ ), but weaker than during the negative half-cycle. For the remainder of the positive half-cycle no further substantial velocity variation was measured.

For the position aligned on a tip (serrated design) and for the linear design, the  $W$ -velocity was minute throughout almost the whole cycle. However, a slight increase, followed immediately by a decrease of the same strength, was observed during the active part of the positive cycle ( $210^\circ$ ). This fluctuation could be due to the reversal motion of charged species at the surface after the voltage reversed. Figure 14(b) shows the absolute velocity for the positions on either side of a tooth. The absolute velocity was considered in this case since the transverse velocity was either positive or negative (the tooth tip was the reference position). The transverse velocity was accelerated during the active part of both negative and positive

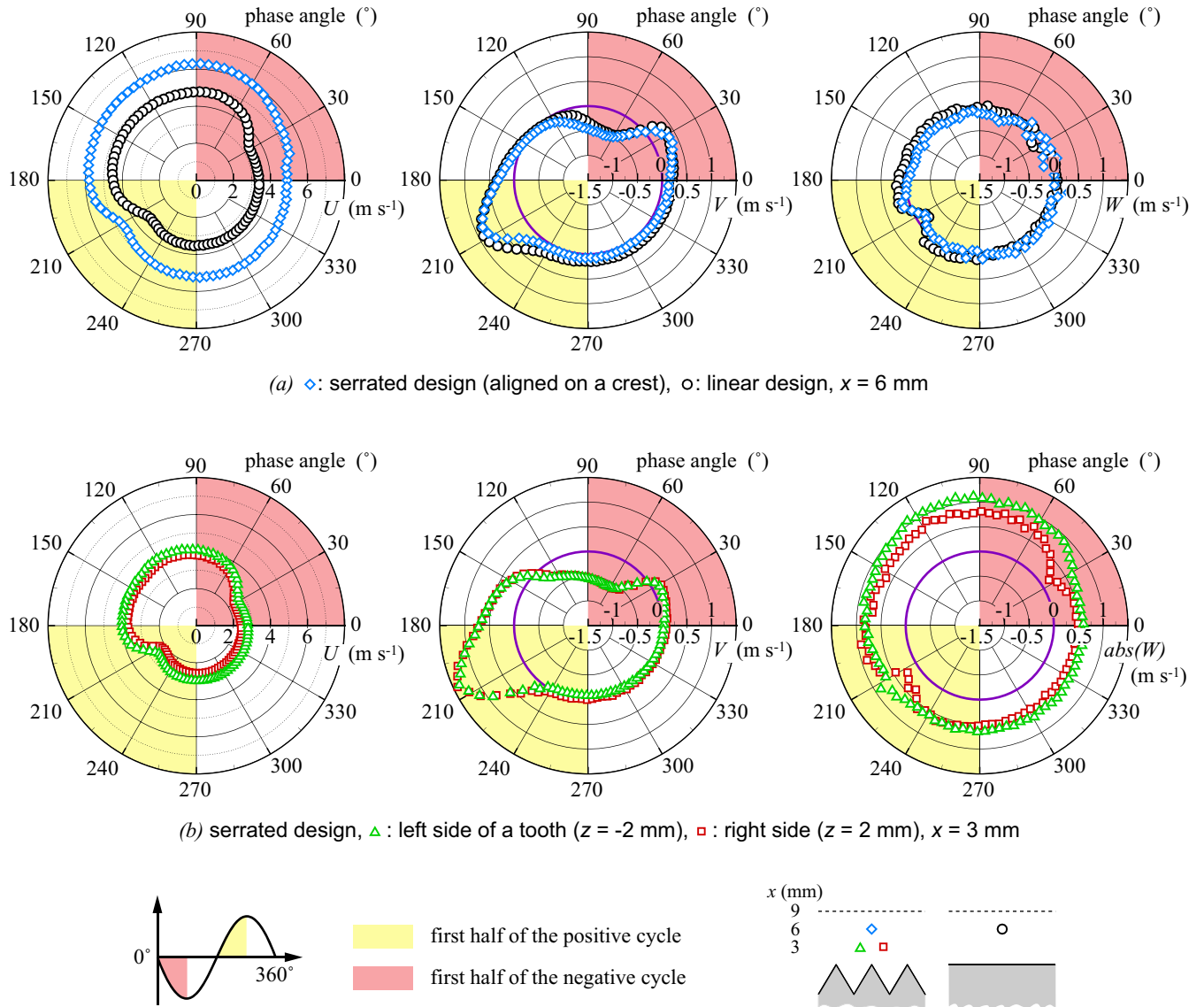


**Figure 14.** Phase-averaged profiles of  $U$ ,  $V$  and  $W$ -velocity (left to right) as a function of the phase angle of the voltage signal at  $y = 0.5$  mm,  $V_{HV} = 10$  kV and  $f_{HV} = 1$  kHz. Panel (a) is related to measurement for the serrated (tip-aligned,  $z = 0$  mm) and linear designs at  $x = 6$  mm and panel (b) is related to measurement for the serrated design on either side of a tip ( $z = \pm 2$  mm) at  $x = 3$  mm. The absolute velocity  $|W|$  is considered for the positions at  $z = \pm 2$  mm.

half-cycles. This phase-averaged variation of  $W$ -velocity was similar to that of the  $U$ -velocity, except in amplitude.

These measurements showed that all the velocity components had a phase-locked variation. For the serrated design,  $U$ - and  $W$ -velocity evolved with similar patterns for the positions not aligned on the tooth tips. The acceleration during the negative half-cycle was higher than the one during the positive half-cycle. When these accelerations occurred, at the beginning of each half-cycle, the  $V$ -velocity was oriented either towards the dielectric surface or upwards.

### 5. Conclusion

This paper focused on the study of the serrated plasma actuator configuration, which had an exposed electrode with a sawtooth edge. This design was compared with the standard one, with strip electrodes. The serrated design induced a slightly

higher power consumption than the linear design. This was related to the serration that increased the area of the plasma for the same applied voltage. This increase was confirmed with images of the discharge which showed longer filaments. During the active phase of the positive and negative half-cycles, streamers and corona spots were, respectively, ignited on the dielectric surface, for both designs. The serration and the repetitive pattern induced, respectively, longer and more curved filaments than the linear design.

The modification of the plasma morphology due to serration had a dominant influence on the induced flow topology. This was first revealed by carrying out friction line visualizations which revealed separatrices on the dielectric surface. The measurements of the three velocity components confirmed the three-dimensional topology induced by the serrated design. The transverse velocity had the same order of magnitude as the vertical one, and had a spanwise periodicity,

implying that vorticity was created between each tip and root, and propagated downstream. Serration induced a higher longitudinal velocity than the linear design. In addition, the acceleration length was increased, since longer filaments were generated. The temporal behaviour of the induced flow was also investigated. For both designs, the longitudinal velocity was higher during the negative half-cycle than during the positive one. For a longitudinal position aligned on a tip, the transverse velocity was negligible. However, for the positions on either side of a tooth, the transverse velocity had, qualitatively, the same phase-locked variation as the longitudinal velocity.

A single plasma actuator with a serrated design is thus able to induce a three-dimensional flow, and more specifically spanwise-periodic vorticity, in the same way as yawed DBD actuators [39] or a plasma actuator array [40] dedicated to reduce flow separation by vortex generation or to delay the laminar-to-turbulent transition of a boundary layer, respectively. Indeed, in this latter flow control application, the spanwise wavelength of the induced vorticity is useful to act on transverse flow disturbances. However, with the actuator design presented in this paper, as the transverse velocity levels remain low in comparison with the longitudinal velocity, no well-established counter-rotating vortices are formed. For that reason, further experiments have to be carried out in order to increase the transverse velocity by optimizing the tooth design (i.e. height and spanwise length) because this ability to create velocity simultaneously in the three directions may be helpful to perform different flow control strategies.

## Acknowledgments

The authors gratefully thank Patrick Gillieron (Renault SAS) who made the 3D-LDV system available. The authors also acknowledge Jean Stefanini (TSI France Inc.) for his technical assistance for the velocity measurements. The authors would furthermore like to acknowledge the constructive feedback from the reviewers.

## References

- [1] Moreau E 2007 Airflow control by non-thermal plasma actuators *J. Phys. D: Appl. Phys.* **40** 605–36
- [2] Corke T C, Enloe C L and Wilkinson S P 2010 Dielectric barrier discharge plasma actuators for flow control *Annu. Rev. Fluid Mech.* **42** 505–29
- [3] Forte M, Jolibois J, Pons J, Moreau E, Touchard G and Cazalens M 2007 Optimization of a dielectric barrier discharge actuator by stationary and non-stationary measurements of the induced flow velocity: application to airflow control *Exp. Fluids* **43** 917–28
- [4] Enloe C L, Corke T C, Haddad O, Jumper E, Kachner K, McLaughlin T E, Post M, and Van Dyken R 2004 Mechanisms and responses of a dielectric barrier plasma actuator: geometric effects *AIAA J.* **42** 595–604
- [5] Van Dyken R, McLaughlin T E and Enloe C L 2004 Parametric investigations of a single dielectric barrier plasma actuator *AIAA Paper No* 2004–846
- [6] Thomas F O, Corke T C, Iqbal M, Kozlov A and Schatzman D 2009 Optimization of dielectric barrier discharge plasma actuators for active aerodynamic flow control *AIAA J.* **47** 2169–78
- [7] Dong B, Bauchire J M, Pouvesle J M, Magnier P and Hong D 2008 Experimental study of a DBD surface discharge for the active control of subsonic airflow *J. Phys. D: Appl. Phys.* **41** 155201
- [8] Pons J, Moreau E and Touchard G 2005 Asymmetric surface dielectric barrier discharge in air at atmospheric pressure: electrical properties and induced airflow characteristics *J. Phys. D: Appl. Phys.* **38** 3635–42
- [9] Jolibois J, Zouzou N, Moreau E and Tatibouët J-M 2011 Generation of surface dbd on rough dielectric: Electrical properties, discharge-induced electric wind and generated chemical species *J. Electrostat.* **69** 522–8
- [10] Hoskinson A R, Hershkowitz N and Ashpis D E 2008 Force measurements of single and double barrier dbd plasma actuators in quiescent air *J. Phys. D: Appl. Phys.* **41** 245209
- [11] Benard N, Mizuno A and Moreau E 2009 A large-scale multiple dielectric barrier discharge actuator based on an innovative three-electrode design *J. Phys. D: Appl. Phys.* **42** 235204
- [12] Abe T, Takizawa Y, Sato S and Kimura N 2008 Experimental study for momentum transfer in a dielectric barrier discharge plasma actuator *AIAA J.* **46** 2248–56
- [13] Roy S and Wang C C 2009 Bulk flow modification with horseshoe and serpentine plasma actuators *J. Phys. D: Appl. Phys.* **42** 032004
- [14] Wang C C and Roy S 2009 Flow shaping using three-dimensional microscale gas discharge *Appl. Phys. Lett.* **95** 081501
- [15] Hoskinson A R and Hershkowitz N 2010 Differences between dielectric barrier discharge plasma actuators with cylindrical and rectangular exposed electrodes *J. Phys. D: Appl. Phys.* **43** 065205
- [16] Liu Z, Wang L and Fu S 2011 Study of flow induced by sine wave and saw tooth plasma actuators *Sci. China Ser. G* **54** 2033–9
- [17] Balcon N, Benard N, Lagmich Y, Boeuf J P, Touchard G and Moreau E 2009 Positive and negative sawtooth signals applied to a DBD plasma actuator - influence on the electric wind *J. Electrostat.* **67** 140–5
- [18] Kotsonis M and Ghaemi S 2012 Performance improvement of plasma actuators using asymmetric high voltage waveforms *J. Phys. D: Appl. Phys.* **45** 045204
- [19] Berendt A, Podliński J and Mizeraczyk J 2011 Comparison of airflow patterns produced by dbd actuators with smooth or saw-like discharge electrode *J. Phys.: Conf. Ser.* **301** 012018
- [20] Wang C C, Durscher R and Roy S 2011 Three-dimensional effects of curved plasma actuators in quiescent air *J. Appl. Phys.* **109** 083305
- [21] Durscher R and Roy S 2012 Three-dimensional flow measurements induced from serpentine plasma actuators in quiescent air *J. Phys. D: Appl. Phys.* **45** 035202
- [22] Jousset R, Leroy A, Weber R, Podliński J and Hong D 2012 Three-dimensional ionic wind induced by dbd plasma actuator using serrated design electrode *Proc. 2012 Int. Symp. on Electrohydrodynamics (Gdansk, Poland, 23–26 September 2012)*
- [23] Laurentie J C, Jolibois J and Moreau E 2009 Surface dielectric barrier discharge: Effect of encapsulation of the grounded electrode on the electromechanical characteristics of the plasma actuator *J. Electrostat.* **67** 93–8
- [24] Kriegseis J, Möller B, Grundmann S and Tropea C 2010 Capacitance and power consumption quantification of dielectric barrier discharge (DBD) plasma actuators *J. Electrostat.* **69** 302–12
- [25] Boucinha V, Jousset R, Magnier P, Leroy-Chesneau A, Weber R, Dong B and Hong D 2008 Characterization of the ionic wind induced by a sine dbd actuator used for

- laminar-to-turbulent transition delay *AIAA Paper No 2008-4210*
- [26] Tropea C, Yarin A L and Foss J F 2007 *Handbook of Experimental Fluid Mechanics* (Berlin: Springer)
- [27] George W K, Beuther P D and Lumley J L 1978 Processing of random signals *Proc. Dynamic Flow Conf. (Skovlunde, Denmark, September 1978)* pp 757–800
- [28] Durscher R and Roy S 2012 Evaluation of thrust measurement techniques for dielectric barrier discharge actuators *Exp. Fluids* **53** 1165–76
- [29] Anne-Archard D, Du Colombier D, Boisson H and Herbert V 2006 Analyse des enduits de visualisation pariétale utilisés en aérodynamique *41ième Colloque National du Groupe Français de Rhéologie (Cherbourg, France, 18–20 Octobre 2006)*
- [30] Perry A E and Chong M S 1987 A description of eddying motions and flow patterns using critical-point concepts *Annu. Rev. Fluid Mech.* **19** 125–55
- [31] Delery J M 1992 Separation and vortex formation in turbulent flows *ONERA, TP No 1992-7*, p 10
- [32] Orlov D M, Font G I and Edelstein D 2008 Characterization of discharge modes of plasma actuators *AIAA J.* **46** 3142–8
- [33] Enloe C L, McHarg M G and McLaughlin T E 2008 Time-correlated force production measurements of the dielectric barrier discharge plasma aerodynamic actuator *J. Appl. Phys.* **103** 073302
- [34] Leonov S B, Yarantsev D A, Gromov V G and Kuriachy A P 2005 Mechanisms of flow control by near-surface electrical discharge generation *AIAA Paper No 2005-780*
- [35] Roth J R and Dai X 2006 Optimization of the aerodynamic plasma actuator as an electrohydrodynamic (EHD) electrical device *AIAA Paper No 2006-1203*
- [36] Kriegseis J, Grundmann S and Tropea C 2011 Power consumption, discharge capacitance and light emission as measures for thrust production of dielectric barrier discharge plasma actuators *J. Appl. Phys.* **110** 013305
- [37] Kotsonis M and Ghaemi S 2011 Forcing mechanisms of dielectric barrier discharge plasma actuators at carrier frequency of 625 Hz *J. Appl. Phys.* **110** 113301
- [38] Enloe C L, McLaughlin T E, Gregory J W, Medina R A and Miller W S 2008 Surface potential and electric structure in the aerodynamic plasma actuator *AIAA Paper No 2008-1103*
- [39] Jukes T N and Choi K-S 2012 Dielectric-barrier-discharge vortex generators: characterisation and optimisation for flow separation control *Exp. Fluids* **52** 329–45
- [40] Hanson R E, Lavoie P, Naguib A M and Morrison J F 2010 Transient growth instability cancellation by a plasma actuator array *Exp. Fluids* **49** 1339–48